Accurate virus identification with interpretable Raman signatures by machine learning

Jiarong Ye[a], Yin-Ting Yeh[b], Yuan Xue[c], Ziyang Wang[d], Na Zhang[b], He Liu[b], Kunyan Zhang[d], RyeAnne Ricker[e,f], Zhuohang Yu[b], Allison Roder[f], Nestor Perea Lopez[b], Lindsey Organtini[g], Wallace Greene[h], Susan Hafenstein[g], Huaguang Lu[i], Elodie Ghedin[f], Mauricio Terrones[b], Shengxi Huang[d], and Sharon Xiaolei Huang[a,1]

Rapid identification of newly emerging or circulating viruses is an important first step toward managing the public health response to potential outbreaks. A portable virus capture device, coupled with label-free Raman spectroscopy, holds the promise of fast detection by rapidly obtaining the Raman signature of a virus followed by a machine learning (ML) approach applied to recognize the virus based on its Raman spectrum, which is used as a fingerprint. We present such an ML approach for analyzing Raman spectra of human and avian viruses. A convolutional neural network (CNN) classifier specifically designed for spectral data achieves very high accuracy for a variety of virus type or subtype identification tasks. In particular, it achieves 99% accuracy for classifying influenza virus type A versus type B, 96% accuracy for classifying four subtypes of influenza A, 95% accuracy for differentiating enveloped and nonenveloped viruses, and 99% accuracy for differentiating avian coronavirus (infectious bronchitis virus [IBV]) from other avian viruses. Furthermore, interpretation of neural net responses in the trained CNN model using a full-gradient algorithm highlights Raman spectral ranges that are most important to virus identification. By correlating ML-selected salient Raman ranges with the signature ranges of known biomolecules and chemical functional groups—for example, amide, amino acid, and carboxylic acid—we verify that our ML model effectively recognizes the Raman signatures of proteins, lipids, and other vital functional groups present in different viruses and uses a weighted combination of these signatures to identify viruses.

Raman spectroscopy | interpretable machine learning | virus identification

Viral outbreaks can spread very quickly through various populations and lead to epidemics and, in some cases, pandemics. Seasonal influenza (FLU) takes an estimated 389,000 lives globally each year (1), and the SARS-CoV-2 pandemic that began in late 2019 has caused more than 167 million infections and over 3.46 million reported deaths globally (2). These infections also come at a tremendous cost to the global economy and threaten to overwhelm healthcare systems. Therefore, it is critically essential to predict, monitor, and control virus infection outbreaks in a timely manner and by accurately identifying emerging virus strains.

In the case of an outbreak, rapid identification and detection is often the first step for an effective public health response (3). Once a pathogen has been identified, PCR diagnostic testing is often the gold standard to detect viruses, as it provides high sensitivity and high specificity. However, the turnaround time, often of several hours, and the fact that it requires targeted detection makes it a limited approach for a rapid response. Rapid tests based on antigen detection have a quick turnaround time of a few minutes, but sensitivity is often low. The ideal setup for rapid diagnostics as well as early detection of new circulating virus types, subtypes, or antigenic variants to inform surveillance and vaccine development is a platform that employs little preprocessing of the samples and has fast, unbiased, and sensitive detection capabilities.

A handheld device that could be taken into the field or clinics would be extremely powerful and would quickly become the standard approach for virus surveillance. The prototype of such a portable device, known as VIRRION (Virus capture with Rapid Raman spectroscopy detection and Identification), was previously proposed (4). It is based on a microfluidic platform containing carbon nanotube (CNT) arrays for label-free capture and enrichment of viruses from clinical samples coupled with an optical detection technology using surface-enhanced Raman spectroscopy that is sensitive to surface proteins and other components of viruses. The input to such a device can be virus cultures, saliva, nasal washes, or even exhaled breath. The output of the device is the Raman spectra of captured viruses. Combining the device with advanced machine learning (ML) models

Significance

A large Raman dataset collected on a variety of viruses enables the training of machine learning (ML) models capable of highly accurate and sensitive virus identification. The trained ML models can then be integrated with a portable device to provide real-time virus detection and identification capability. We validate this conceptual framework by presenting highly accurate virus type and subtype identification results using a convolutional neural network to classify Raman spectra of viruses. The accurate and interpretable ML model developed for Raman virus identification presents promising potential in a real-time, label-free virus detection system that could be used in future outbreaks and pandemics.

[1]To whom correspondence may be addressed. Email: suh972@psu.edu.

that can classify these spectra to identify the type, subtype, and strain of captured viruses promises an innovative system that can quickly detect, track, and monitor viral outbreaks in real time.

ML has been successfully applied to Raman spectroscopy analysis in various application scenarios, such as cancer detection (5) and bacteria classification (6). One limitation of current ML-based spectra analysis methods is the lack of transparency in the decision-making process and lack of interpretation of the ML models. Although high accuracy is often reported, the trained ML models, especially those based on deep learning (1), are not transparent and do not provide insight into why and how such accuracy is achieved. One approach to enhance transparency is to develop ML models that highlight salient features used for virus identification and then correlate such ML-selected features (e.g., Raman wavenumber ranges) with the Raman signatures of biomolecules known to exist in viruses such as proteins and lipids (7, 8). A previous study has shown that FLU viruses can be identified by Raman signals generated by surface proteins and lipids (9). Another study on SARS-CoV-2 detected peaks corresponding to the spike protein using Raman spectroscopy (10). However, these existing studies lack quantitative analyses and peak-matching to functional groups (11–13).

In this work, we aim to develop a highly accurate and interpretable ML framework for virus identification based on Raman spectra. We propose a one-dimensional (1D) convolutional neural network (CNN) that is specifically designed to extract multiscale features from 1D Raman spectra and perform classification based on the extracted features. Compared to existing ML models, our 1D CNN model is made more interpretable for Raman spectra analysis by incorporating a full-gradient algorithm that calculates a "feature importance map," which shows the relative importance of wavenumbers in recognizing the corresponding virus types of input spectra. When tested on our dataset of virus Raman spectra, the CNN model achieves at least 95% accuracy for classifying different types of FLU virus and different subtypes of influenza A (FLUA) virus, differentiating enveloped from nonenveloped viruses, and differentiating avian coronavirus (infectious bronchitis virus [IBV]) from other avian viruses. The wavenumbers (or Raman features) highlighted by the CNN-calculated feature importance map can also inform us on what virus features Raman spectroscopy detects and ML employs for identification. To better understand the molecular basis of Raman detection, we gathered information from the literature on Raman signatures of protein-related functional groups such as amide, amino acid, carboxylic acid, lipids, and lipid-related functional groups such as aliphatic chains (7, 8, 14) and collected data in our own set of experiments using protein domains of interest. We find that these known signature ranges correlate well with the key Raman frequency ranges located by our CNN-based ML model. We also designed a quantifiable metric to measure the level of correlation between the ML-selected ranges and the signature ranges of specific biomolecules.

Results

A schematic demonstration of the VIRRION platform (4) for label-free capture and enrichment of viruses is shown in Fig. 1A. We used the device to acquire a dataset consisting of Raman spectra of three groups of RNA viruses, including human respiratory viruses (FLUA H1N1 and H3N2, influenza B [FLUB], rhinovirus, respiratory syncytial virus [RSV]), avian respiratory viruses (FLUA H5N2 and H7N2, IBV, reovirus), and human

enteroviruses (coxsackievirus B type 1 and 3 [CVB1, CVB3], enteroviruses EV70 and EV71). Details of the virus sample preparation procedures can be found in the Virus samples preparation subsection under the *Materials and Methods* section. ML experiments were then conducted using this dataset of Raman spectra of viruses. Fig. 1B shows the architecture of our proposed 1D CNN (1D-CNN) for classification of virus spectra and illustrates the idea that our ML framework can be applied to interpret Raman wavenumber ranges important to ML classification with respect to their correlation with Raman peak ranges of various biomolecules existing in viruses.

Virus Raman Spectra Data Preprocessing and Augmentation. Before feeding the Raman spectra into ML classifiers as input, it is essential to employ a few preprocessing steps to reduce noise in the spectra that could potentially undermine the classification performance of trained ML models. One important preprocessing step is baseline correction. We applied the asymmetric least squares smoothing algorithm (15) for baseline correction on each Raman spectrum for all types and subtypes of viruses. In Fig. 2A, we show human FLUA and FLUB example spectra before and after baseline correction. For illustration of the spectrum data distribution after baseline correction, we visualize the FLUA and FLUB spectra using a t-distributed stochastic neighbor embedding (t-SNE) (16) plot (Fig. 2B). In *SI Appendix*, Fig. S1, we further compare the t-SNE plots before and after baseline correction for all spectra of all virus types in our entire dataset. From the comparison, we observe that applying baseline correction makes the spectra of different viruses more distinguishable, which makes it easier to achieve high accuracy in virus classification tasks. More details about the baseline correction algorithm and parameters used for generating the t-SNE plots are explained in the Virus Raman spectra preprocessing subsection under the *Materials and Methods* section.

In Fig. 3, we show the number of Raman spectra for the human respiratory viruses, avian viruses, and human enteroviruses in our dataset. Considering that the number of spectra varies among viruses (indicating the presence of data imbalance), we adopted a data augmentation strategy by random oversampling (17). For any classification task, the oversampling augmentation is implemented for virus types with fewer spectra in the training set by bootstrapping, a statistical technique that samples data with replacement (18), so that after the augmentation, the number of spectra of every virus type matches that of the virus type with the largest number of training spectra for the task.

CNN for Classification of Virus Raman Spectra. To perform virus identification from Raman spectra, we compared the performances of several different ML models including XGBoost (19) and CNN. XGBoost is a popular ML method similar to the Random Forest (20) method. Instead of an ensemble of multiple decision trees in a random forest, XGBoost uses a boosting style ensemble that iteratively builds more decision trees in the learning process. CNN, in comparison, has stronger capability in learning feature representations. However, widely used two-dimensional (2D) convolutional kernels are not appropriate for sequence-like data such as Raman spectra. To this end, we designed a 1D-CNN to extract features from Raman spectra and perform accurate virus identification. Fig. 1B demonstrates the architecture of our proposed 1D-CNN for virus classification using spectra. Inputs to both 1D-CNN and XGBoost are Raman spectra in the format of 1D vectors. Details about the architecture and training process of our CNN classifier can be found in the CNN architecture and
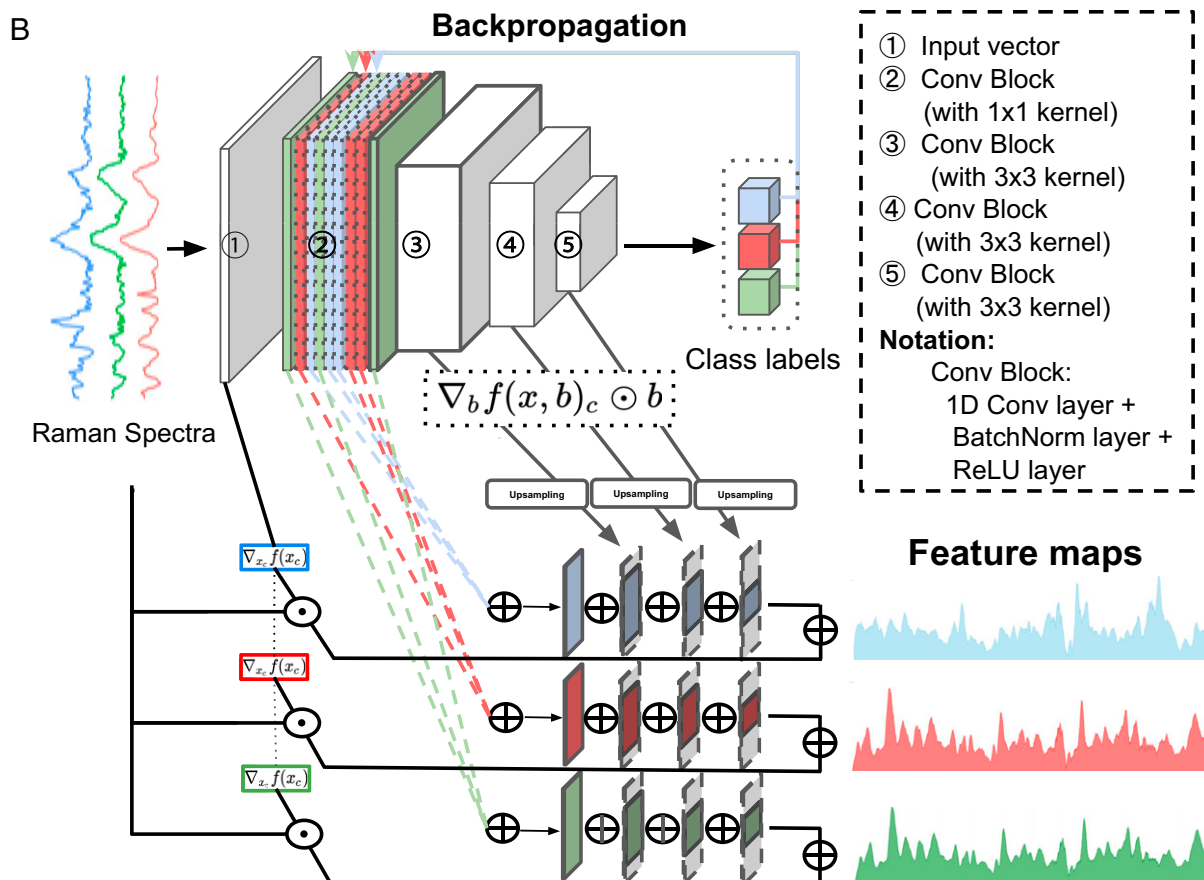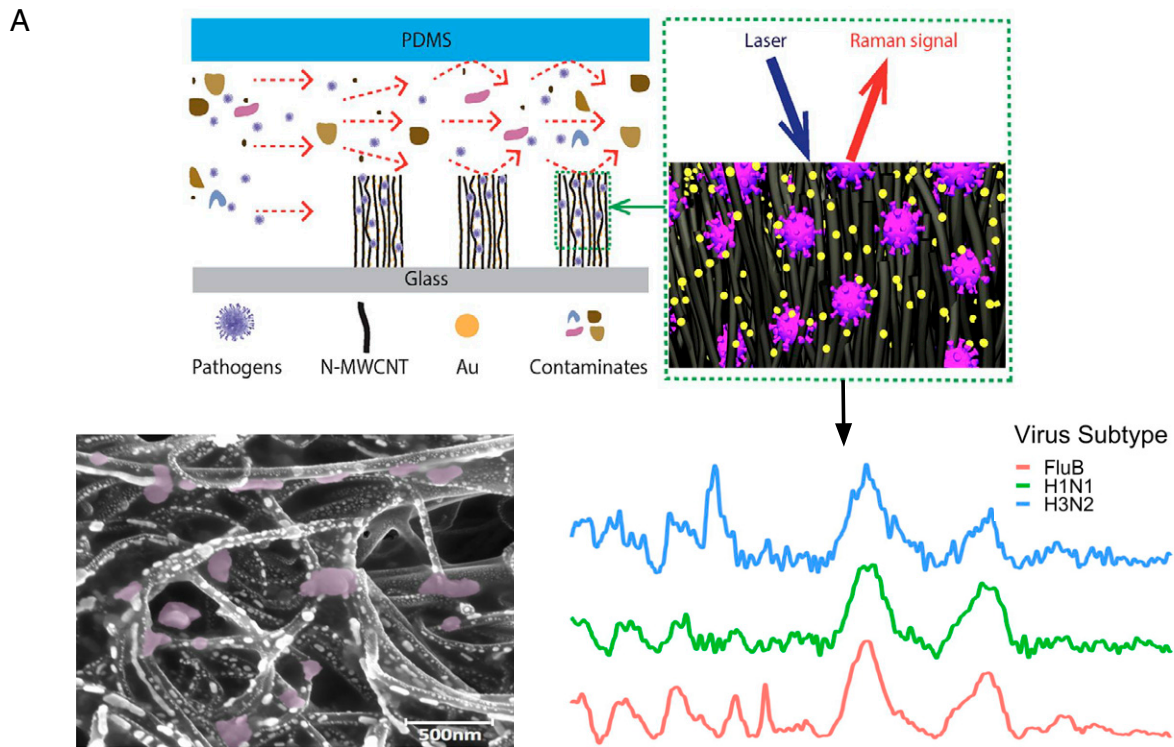
Fig. 1. (*A*) Schematics showing the nitrogen-doped multiwall CNTs device encapsulated in polydimethylsiloxane used to enrich viruses (*Top Left*). The viruses are enriched between CNTs where the Au nanoparticles are predeposited. Raman spectra are then collected from the virus-enriched samples (*Top Right*). A scanning electron microscope image (*Bottom Left*) of a sample shows CNTs, Au nanoparticles, and trapped viruses (purple colored). Raman spectra from different virus samples are shown (*Bottom Right*) (FLUB in red, FLUA H1N1 in green, and FLUA H3N2 in blue). (*B*) The CNN architecture for virus identification and the process of extracting Raman feature maps show important Raman signature ranges. The feature maps extracted are class specific, demonstrating the significant Raman ranges for identifying different virus types (or subtypes, depending on the classification task) in different colors.
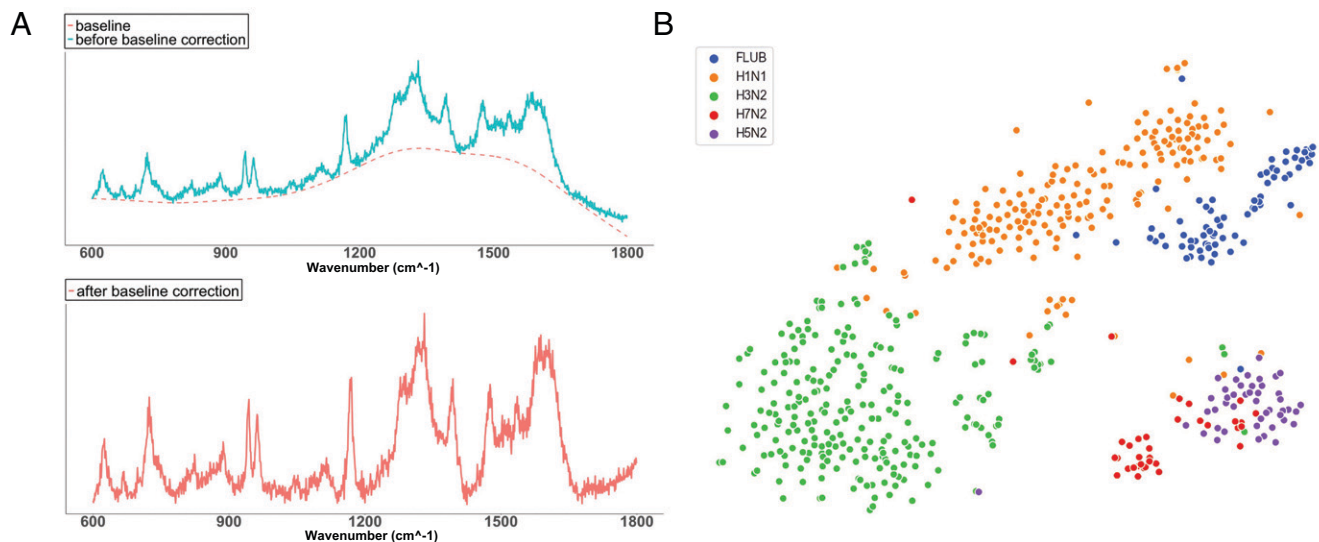
Fig. 2. (*A*) Sample Raman spectra before and after baseline correction. (*B*) T-SNE plot of FLUA subtypes (H1N1, H3N2, H5N2, H7N2) and FLUB after baseline correction.

training details subsection under the Materials and Methods section. For experiments using XGBoost, we kept the built-in default setting of XGBoost (19).

We measured classification performance using three metrics (accuracy, sensitivity, and specificity). The mathematical definitions for these metrics are provided in *SI Appendix,* Table S1. Comparing CNN and XGBoost, our 1D-CNN model achieved better performance in all classification tasks, including virus identification from all possible virus types, differentiating enveloped from nonenveloped viruses, classifying different types of human respiratory viruses, differentiating human FLUA from FLUB viruses, identifying the subtype of FLUA viruses, and classifying avian viruses; Fig. 4 summarizes the classification results. The

actual metric numbers for each virus group and all classification experiments are included in *SI Appendix,* Figs. S2–S7. Among all virus types and subtypes, the CNN classifier achieved the highest identification accuracies for IBV coronavirus and FLUA virus, around 98% and 97%, respectively (*SI Appendix,* Fig. S8).

Interpretation of Salient Raman Ranges Selected by ML. While CNN achieves promising classification results, NNs including CNNs are known to be "black boxes" and often do not provide sufficient explanation for the learned feature representations (21). Recent advances in interpretability of NN models have alleviated this concern by offering numerous ways of visualizing the weights and features within the NN layers (22–27). Here,
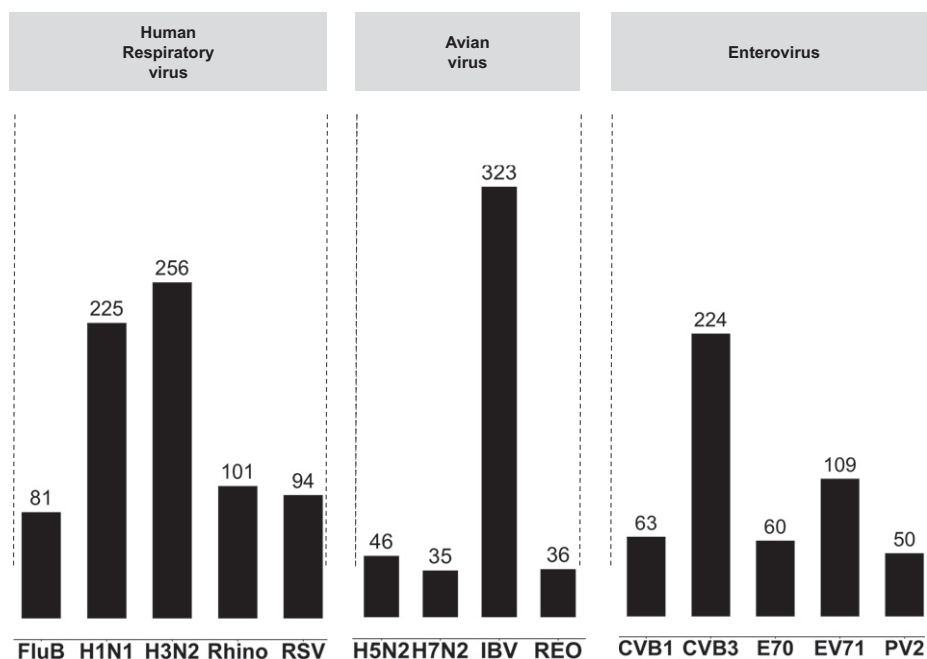

Fig. 3. Number of spectra in our dataset for human respiratory viruses, avian viruses, and human enteroviruses. H1N1, H3N2, H5N2, and H7N2 are subtypes of the FLUA virus; FLUB, influenza B virus; Rhino, rhinovirus; RSV, respiratory syncytial virus; IBV, infectious bronchitis virus; Reo, reovirus; CVB1 and CVB3, coxsackievirus B type 1 and 3; EV70 and EV71, enteroviruses. Numbers above each column indicate the number of spectra collected for each virus. These spectra all have ground truth labels, which are the virus type/subtype. Note that for classification tasks, we apply data augmentation to add more samples to virus classes that have fewer spectra samples so that for each classification task, every virus type has an equal number of spectra samples in the training set.

we propose a method of interpreting our 1D-CNN decision-making process by calculating a "feature importance map," which shows the relative importance of wavenumbers in recognizing the corresponding virus types of input spectra. The wavenumbers (or features) with the highest importance values can tell us what virus features Raman spectroscopy detects that ML uses to identify the viruses. The calculation of the feature importance map is based on a full-gradients algorithm (28), as illustrated in the overview diagram Fig. 1*B* and detailed in the Calculation of Raman feature importance maps using CNN responses subsection under the *Materials and Methods* section.

The feature importance map allows us to identify Raman signature ranges deemed most important by the CNN classifier for virus identification. We can then correlate these ML-selected salient Raman ranges with the signature peak ranges of known biomolecules and chemical functional groups such as lipids, proteins, nucleic acids, amino acids, and amide to seek insights into what differences in biomolecular composition among viruses are captured in the Raman spectra and then used by ML to recognize viruses.

To measure the level of correlation between the ML-selected important wavenumber ranges and Raman peak wavenumber ranges of a known biomolecule, we propose a quantifiable metric termed "matching score." It is a ratio with the numerator as the range of overlapped wavenumbers between ML-determined important ranges and Raman peak ranges of the biomolecule and the denominator as the total Raman peak ranges of that biomolecule (Fig. 5). The higher the matching score, the more likely the signatures of the biomolecule contribute substantially to distinguish viruses. Using this quantifiable metric, we can make some educated guesses about the relative importance of biomolecules in virus identification tasks. Details of this algorithm for measuring correlation can be found in the Interpretable Raman signatures subsection under the *Materials and Methods* section.

In Figs. 6–8, we show example feature importance maps from CNN and their correlation with Raman peak ranges of biomolecules known to exist in viruses. In choosing which biomolecules and functional groups to evaluate, we used prior knowledge about the composition of the RNA viruses in our study. Some viruses are enveloped (FLUA and FLUB, IBV coronavirus, RSV), and some are not (reovirus, enterovirus CVB1/CVB3/EV70/EV71/PV2, rhino); thus, we included lipid as one type of biomolecule to evaluate since the envelope is formed by the cell-surface lipid bilayers. We also included surface protein-related functional groups and individual amino acids, such as amide, phenylalanine, and tyrosine. Phenylalanine and tyrosine are chosen because of reports that they are present and important in respiratory viruses (29–33). RNA is also included because all viruses tested here have RNA genomes. Details about how we obtained the Raman peak ranges for the biomolecules and functional groups under consideration are available in the Interpretable Raman signatures subsection under the Materials and Methods section. Next, we
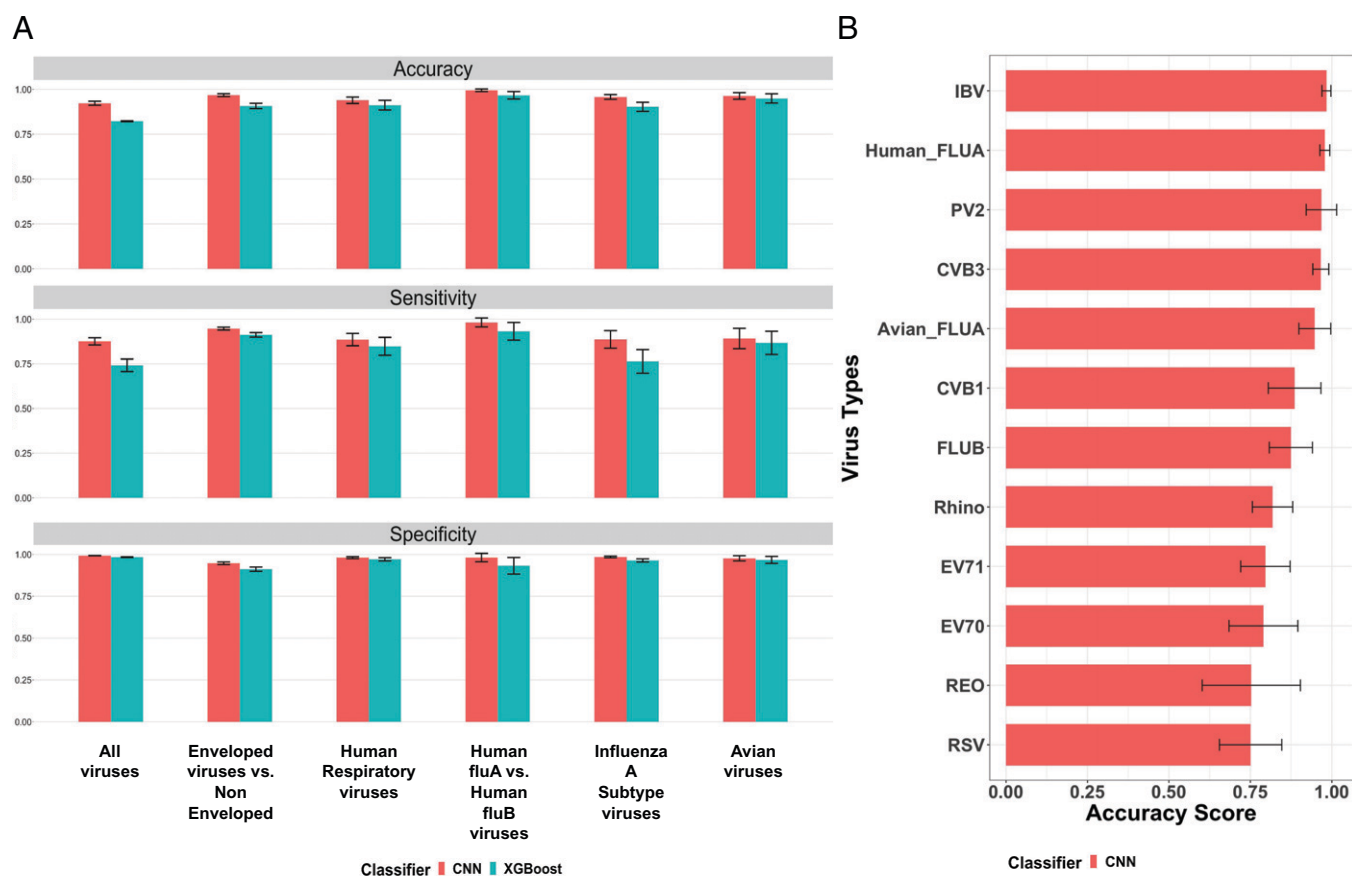

Fig. 4. (*A*) The classification performance of our CNN model and the XGBoost model on six experiments: 1) all viruses (classification of all virus types): avian, enteroviruses, human respiratory viruses; 2) enveloped viruses versus nonenveloped: FLUA and FLUB, IBV coronavirus, and RSV are enveloped, and reovirus, enterovirus CVB1/CVB3/EV70/EV71/PV2, and rhino are nonenveloped; 3) human respiratory viruses; 4) human FLUA versus human FLUB viruses; 5) FLUA subtypes; and 6) avian viruses. Three metrics (accuracy, sensitivity, and specificity) are measured for both classification models. Results for all metrics are obtained by running a 5-fold cross-validation five times for fair comparison (each error bar represents the SD of the corresponding metric score for each experiment across 5-fold cross-validation in five tests). (*B*) Accuracy score for every virus type in the all-viruses classification task (each error bar represents the SD of the corresponding accuracy score for each virus type across 5-fold cross-validation in five tests).
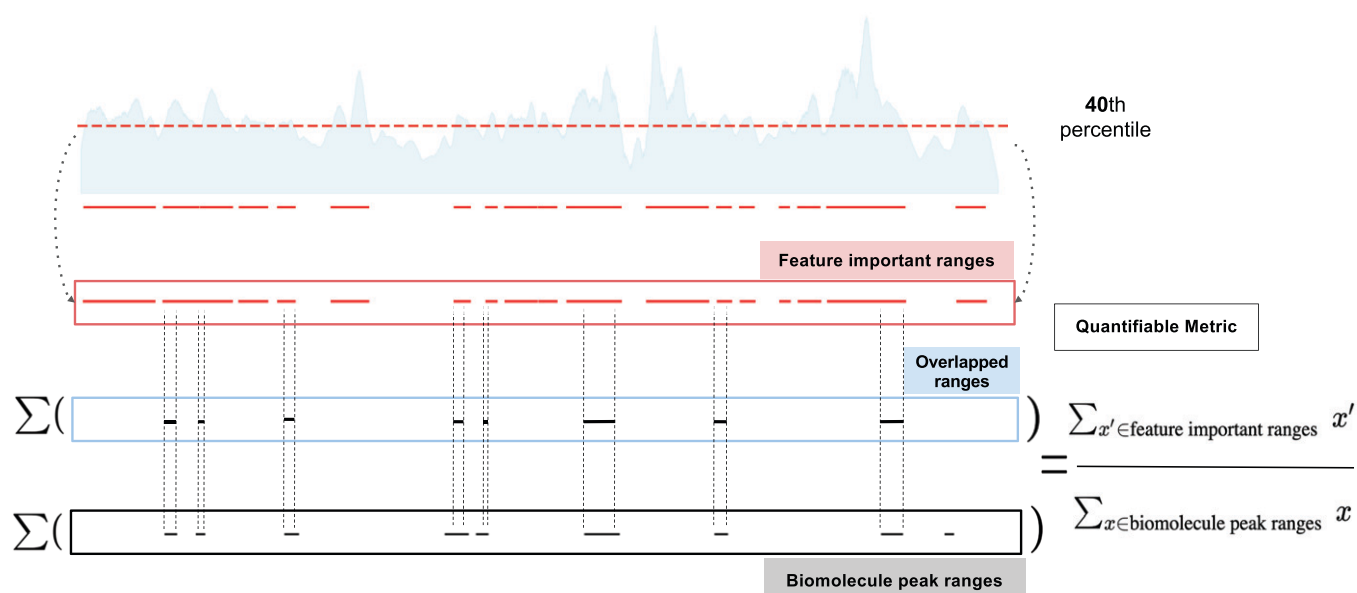
Feature Map of Virus Type/Subtype

Fig. 5. Illustration of the quantifiable matching score calculation leveraging biomolecule peak ranges and important ranges extracted from ML-calculated feature maps of each virus type (or subtype, depending on the classification task). A threshold of 40th percentile is applied to the ML-calculated feature importance map so that Raman bands with importance scores below the threshold are discarded, and the remaining wavenumbers above the threshold are considered as important Raman ranges for identifying the virus based on ML and can then be correlated with biomolecule peak ranges.

calculated the matching scores between ML-selected important Raman ranges and biomolecule peak ranges for various virus classification tasks.

Enveloped versus nonenveloped virus classification. We did an experiment to train an ML model to classify enveloped versus nonenveloped viruses and achieved very high accuracy (94.8% accuracy; *SI Appendix,* Fig. S6). This ML model could be used for fast screening to identify whether a new virus is enveloped or nonenveloped. In Fig. 6, we show the Raman feature importance map calculated by this ML model as well as matching scores between ML-selected important ranges and biomolecular peak ranges. From the matching score table, one can see that for this task, lipid is shown to be much more important (matching score of 51.98%) than protein-related functional groups (matching scores of 25% and 7.98% for amide I and amide III, respectively). This is consistent with the difference between enveloped and nonenveloped viruses, which is that enveloped viruses have an enclosing phospholipid bilayer, whereas nonenveloped viruses do not have the phospholipid bilayer. It is highly likely that the ML model is picking up the signature ranges of lipid to differentiate enveloped from nonenveloped viruses.

Comparison of classification tasks that differentiate various flu types and subtypes. We trained several ML models to differentiate FLU viruses such as avian FLUA from human FLUA and human FLUA from human FLUB (Fig. 7 and *SI Appendix,* Fig. S5). From the matching score table, we noted that the amide III range is not important for classifying avian FLUA versus human FLUA (matching score of 13.16%) but more important when differentiating human FLUA from human FLUB (matching score of 73.68%). Lipid is more important when differentiating avian FLUA from human FLUA but less important when differentiating human FLUA from human FLUB, likely indicating that the ML model trained for classifying avian FLUA versus human FLUA is capturing their differences in the envelopes since the phospholipid bilayer of the human viruses comes from different cells than the avian viruses that were isolated in eggs. Also,

the RNA matching score stands out to be higher (60%) when differentiating human FLUA from human FLUB, compared to classifying avian FLUA versus human FLUA (40%). In another experiment, we trained an ML model to differentiate four subtypes of FLUA, human H1N1 and H3N2, and avian H5N2 and H7N2 (*SI Appendix,* Fig. S4). Again, we observe that lipid is important, whereas amide III is not important when differentiating the FLUA subtypes.

Classification of avian viruses including IBV coronavirus. We trained an ML model to differentiate three types of avian viruses and achieved very high accuracy (99.8%) in identifying the IBV coronavirus (Fig. 8, and *SI Appendix,* Fig. S2). This shows that the Raman spectra of coronavirus have specific signatures that make them easily identifiable when compared to avian FLU. The proposed technique combining Raman spectroscopy and ML could potentially be used for highly reliable detection and identification of coronaviruses. From the matching score table shown in Fig. 8, one can see that both lipid and protein peak ranges have high correlation with ML-selected important Raman ranges for distinguishing IBV coronavirus from other avian viruses, likely indicating that Raman spectroscopy and ML are picking up signatures of the spike protein and receptor binding domains of coronaviruses.

Additional observations about correlation between ML-selected important Raman ranges and biomolecule peak ranges. When comparing the matching scores for the experiment classifying different human respiratory viruses (*SI Appendix,* Fig. S7) and the experiment classifying different subtypes of FLUA (*SI Appendix,* Fig. S4), we observe that 1) the relative importance of lipids is higher in the FLUA subtype identification task, and 2) there is a significant difference in the relative importance of the amide III range. While amide III is very important in respiratory virus classification, it is minimally important in FLUA subtype identification, which could indicate that the spectra of all subtypes of FLUA are very similar in the amide III range. Amide III is a signature Raman band in proteins but can be sensitive to secondary structures, and such a difference of its
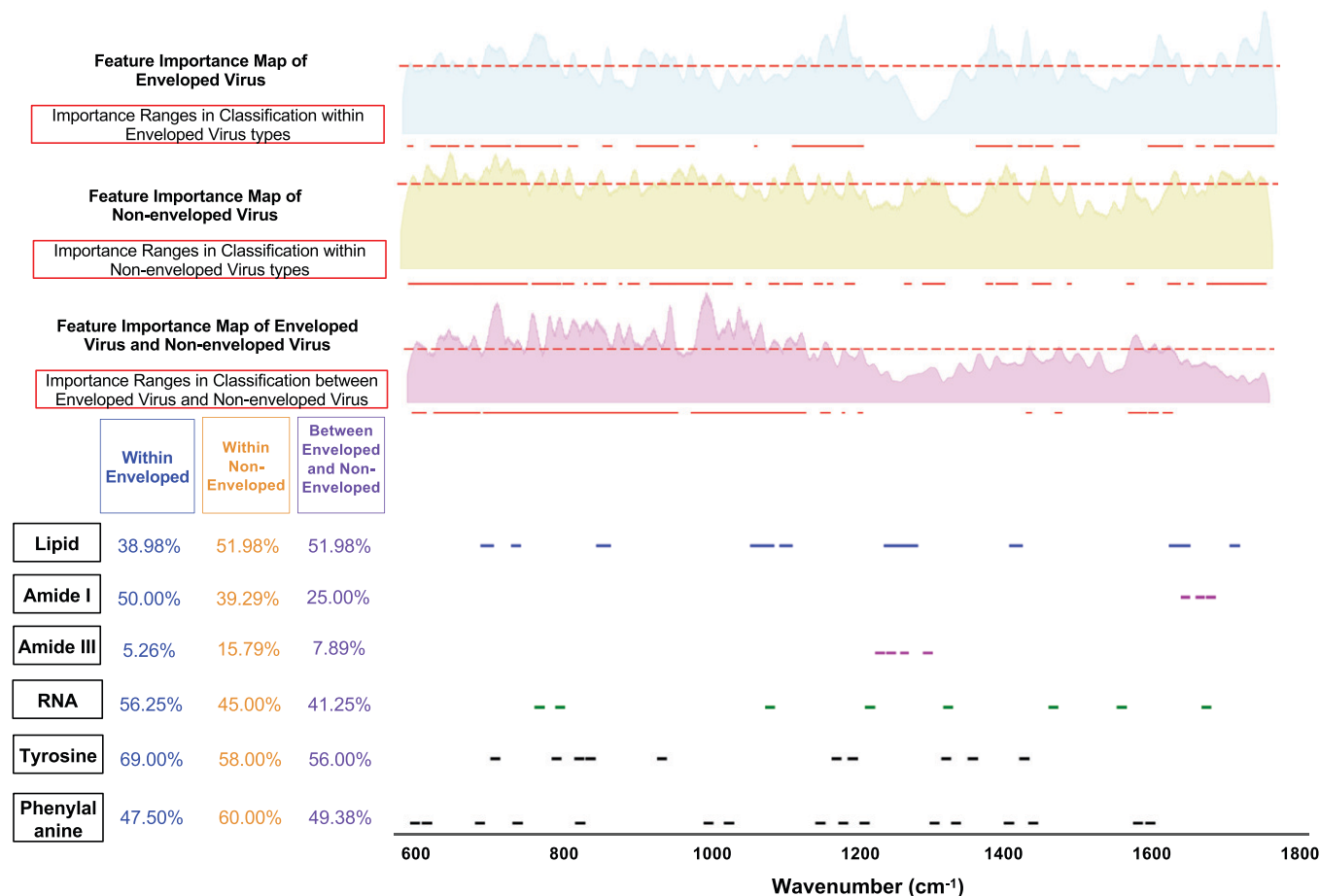
Fig. 6. Biomolecule peak ranges, ML-calculated feature importance map, and important Raman ranges (above 40th percentile threshold) for classification experiments: 1) within enveloped virus types (avian FLUA, IBV coronavirus, human FLUA, human FLUB, RSV); 2) within nonenveloped virus types (enterovirus [CVB1, CVB3, EV70, EV71, PV2], rhino, reovirus); and 3) between enveloped and nonenveloped viruses. Feature importance maps are extracted from intermediate layers of the CNN as described in Fig. 1*B*. The matching score for each classification experiment is calculated by correlating ML-selected important ranges with each biomolecule's known Raman peak ranges. (*SI Appendix*, Fig. S6 includes matching scores with more functional groups).

matching scores indicates that the viruses have different surface proteins (34, 35)—which is, indeed, the case when comparing different families of viruses—and that the subtypes have slight differences in their surface proteins—which, again, is the case since FLUA viruses have hemagglutinin and neuraminidase on their surfaces. This is consistent with our preliminary findings about the viruses under study. We also observe that 3) the two chosen amino acids (phenylalanine and tyrosine) are consistently important in respiratory virus type or subtype classification, and, finally, 4) the RNA genome is also generally important for detecting virus differences by Raman.

Viral Dose Detection Limit. To determine what the viral dose detection limit of our method was, we conducted a series of dilution experiments using a flu virus dataset consisting of Raman spectra of 11 FLU virus strains. Information about this dataset is given in *SI Appendix*, Table S2. Around 10,000 spectra were collected for each virus sample at the original undiluted concentration. For two strains–A/Indiana/08/2018(H3N2) and A/Nebraska/14/2019(H1N1)—we collected spectra at different virus concentrations. The original undiluted viruses were for Indiana/08 at a TCID50 (median tissue culture infectious dose) of 1.45e+07 viruses/mL and an RNA copy number of 1.42e+09/mL, while Nebraska/14 was at a TCID50 of 2.29e+07/mL and an RNA copy number of 2.27e+09/mL Increments of 10-fold dilutions were performed down to 10^{-6} dilution, which corresponded to fewer than one replicating virus and ∼14 RNA copies

per 10 µL solution for Indiana/08 and fewer than one replicating virus and ∼23 RNA copies per 10 µL solution for Nebraska/14. *SI Appendix*, Table S3, displays the expected number of viruses and RNA copies in each 10 µL sample solution used to collect spectra. At each level of dilution, 400 Raman spectra were collected for the corresponding 10 µL solution.

On this dataset, we conducted ML experiments using our proposed CNN model, as shown in Fig. 1*B*, in a blind-testing setting for flu type and subtype classification. Since the two strains being used for testing the viral dose detection limit, Indiana/08 and Nebraska/14, are among the 11 strains in the dataset, we trained our ML model using 9 strains of H1N1, H3N2, and FluB in *SI Appendix*, Table S2, excluding these two testing strains. Then, the spectra of the two testing strains at different dilution levels were classified using the trained ML model as previously unseen strains (i.e., not contained in the training set). The goal was to examine the ML classification performance for spectra collected at different dilutions and, thus, infer the detection limit of our approach. The ML classification results are shown in *SI Appendix*, Table S4. We can observe from the results that our ML model, which was trained on nine strains (not including the two testing strains) using spectra collected at the undiluted concentration only, was able to reliably predict the subtype of the two testing strains using spectra collected at the undiluted and 10^{-1}, 10^{-2}, 10^{-3}, 10^{-4}, 10^{-5} dilutions. At 10^{-6} dilution, however, we start to see unpredictability; in the case of Indiana/08, the percentage of

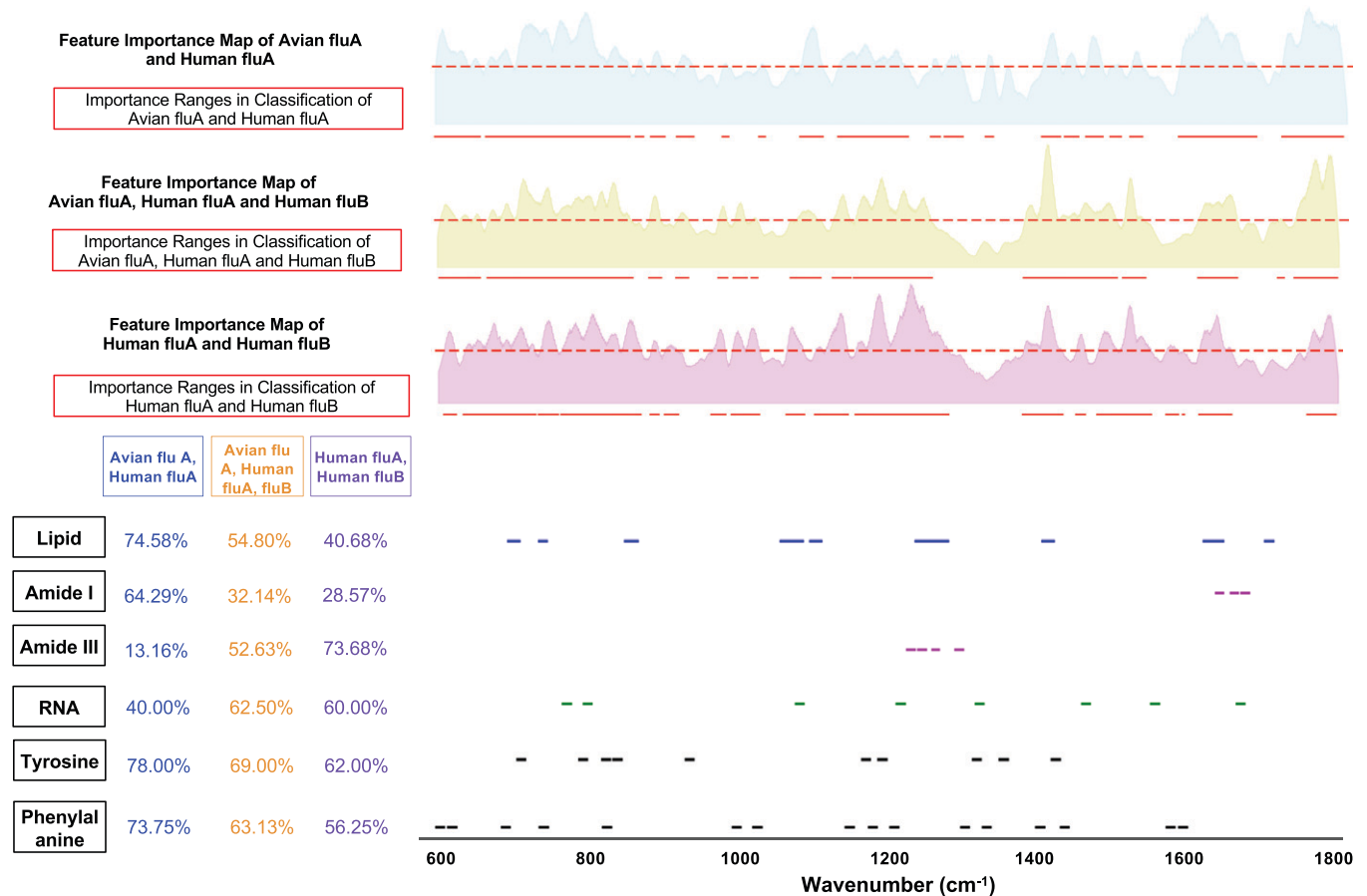|	Avian flu A, Human fluA	Avian flu A, Human fluA, fluB	Human fluA, Human fluB		
Lipid	74.58%	54.80%	40.68%		
Amide I	64.29%	32.14%	28.57%		
Amide III	13.16%	52.63%	73.68%		
RNA	40.00%	62.50%	60.00%		
Tyrosine	78.00%	69.00%	62.00%		
Phenylal anine	73.75%	63.13%	56.25%		

Fig. 7. ML-calculated feature importance map and important Raman ranges for classification experiments: 1) avian FLUA versus human FLUA; 2) avian FLUA, human FLUA, and human FLUB; and 3) human FLUA and human FLUB. (*SI Appendix,* Fig. S5 includes matching scores with more functional groups).

blank spectra among the 400 collected spectra spiked to 90.25%, which means that we had to filter out around 90% of the spectra in order to correctly classify the case; and for Nebraska/14, our model mistakenly classified it to FLUB using spectra collected at 10^{-6} dilution. Therefore, based on this set of experiments, the detection limit of our technique in the present setup is 10^{-5} dilution, which corresponds to roughly one replicating virus and 142 RNA copies per 10 µL for Indiana/08 and roughly two replicating viruses and 227 RNA copies per 10 µL for Nebraska/14 (*SI Appendix,* Table S3).

Discussion

Detecting and classifying virus using the technique presented here is very fast, making it feasible as a real-time, label-free virus screening and detection tool. Once the ML model is trained, it takes ~1e−05 s on an NVIDIA Quadro RTX 6000 GPU with 24 GB RAM. If we are performing case-based experiments (i.e., classifying hundreds of spectra collected for a virus sample to determine the virus label), the run time is still less than a second. The more challenging aspect is whether the detection can extend to viruses not contained in the training set. The blind-testing experiments conducted for determining the viral dose detection limit (*SI Appendix,* Table S4) demonstrate that while the ML model can recognize the type and subtype of a virus not contained in the training set, it may not be able to recognize the specific strain (often determined by the year and region the virus was isolated). The model can still predict the broader category (type, subtype) of a strain in the training set that is recognized as closest to the unseen strain because of the model's

ability to output a probability score and correlate the Raman signature of the testing strain with those of known strains. Being able to detect an unknown strain and interpret its Raman signature is one of our main future research directions. We are investigating zero-shot ML techniques that can be integrated into our ML framework so that our model will be able to either detect a virus strain that is already contained in the training set or predict that the testing virus is of a previously unknown strain and, in such case, interpret its Raman signature in terms of its correlation with the Raman signatures of known viruses, biomolecules, and/or chemical functional groups present in viruses. The expected outcome of such an improved model is that the model will first provide a binary decision regarding whether the testing strain is one of the strains in the training set (i.e., same strain, but different samples). If the strain is recognized as one of those seen ones, its label will be predicted. If the strain is detected as a new strain that is not contained in the training set, the feature importance map output by our model will allow us to examine where (i.e., based on which biomolecules or chemical functional groups) the new strain is different from previously seen strains. The implication is that the model could then predict which existing strains are the closest to the new strain.

The robustness of a virus screening and detection system using our technique can be improved through more robust spectra collection and by refining preprocessing steps to ensure the quality of the spectra used in the ML experiments. A practical system will consist of virus capture and enrichment, spectra collection, and a sequence of preprocessing steps to prune out outlier spectra and remove blank spectra. The remaining Raman
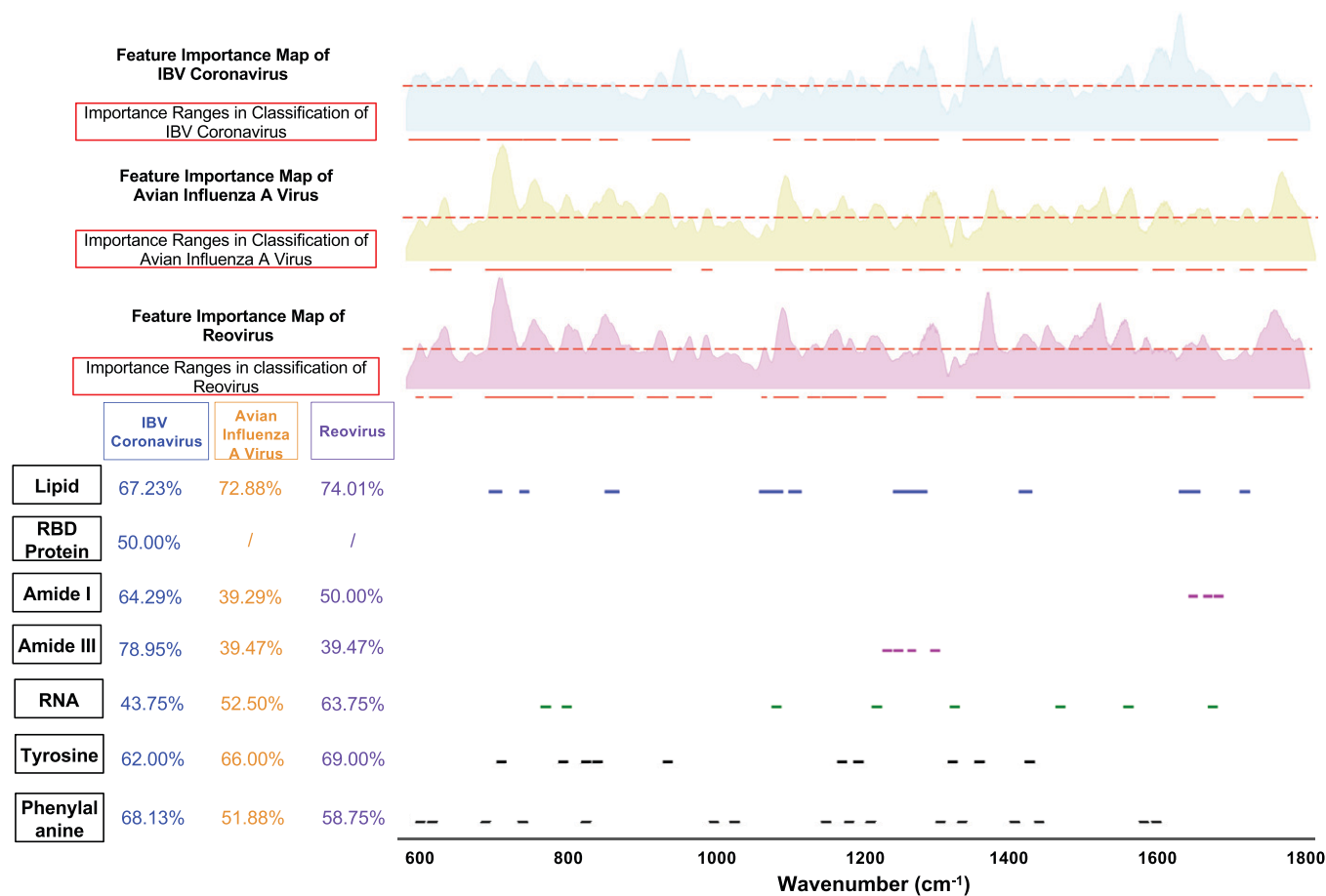
	IBV Coronavirus	Avian Influenza A Virus	Reovirus
Lipid	67.23%	72.88%	74.01%
RBD Protein	50.00%	/	/
Amide I	64.29%	39.29%	50.00%
Amide III	78.95%	39.47%	39.47%
RNA	43.75%	52.50%	63.75%
Tyrosine	62.00%	66.00%	69.00%
Phenylalanine	68.13%	51.88%	58.75%

Fig. 8. ML-calculated feature importance map and important Raman ranges for classifying three types of avian viruses: IBV coronavirus, avian FLUA virus, and reovirus. Feature important maps and matching scores are given for each avian virus type. The matching score for RBD protein only applies when correlating with IBV coronavirus because RBD protein is an exclusive biomolecule in IBV. (*SI Appendix,* Fig. S2 includes matching scores with more functional groups.)

spectra-encoding virus signatures are then classified by the trained ML model to recognize the virus label. One encouraging observation is that adding a preprocessing step to remove blank spectra has been extremely helpful in improving classification performance (*SI Appendix,* Table S4). Note that the blank spectra were identified by a blank-spectra classifier, which was trained using a small dataset of blank spectra collected from only background and no virus. With preprocessing steps such as discarding blank spectra and possibly other outlier spectra with signal from a more "real-life" background media, our technique will be more robust because it can then filter out spectra that do not encode virus signal. The potential of using preprocessing to remove noisy and irrelevant spectra could also explain one phenomenon that we observe from *SI Appendix,* Table S4, which is that the accuracies at more diluted levels from 10^{-1} to 10^{-5} do not decrease and can still be high, maybe because contaminants and background are also being removed at higher dilution. Thus, the remaining spectra being classified by the ML model are "cleaner" virus spectra. This may not be the case in clinical samples with a low concentration of virus, as background molecules, in this case, would not be diluted. However, host contamination (background molecules) would, in principle, get filtered out when run through the CNTs (see ref. 4). Furthermore, preprocessing and filtering steps can be applied to remove spectra resulting from background and leave only spectra with virus signal to be classified by the ML model. While determining how the system reacts with real biological fluids and tissues (e.g., saliva) is of very high interest to us, this represents the next step and goes beyond the scope of our current study.

While the methods we present here are for rapid detection, they are not meant to replace PCR, which is a highly specific and sensitive method for the detection of known viruses (36). Our goal was to develop an ML approach to better mine the spectra from Raman spectroscopy for rapid and label-free detection of viruses. In the process, we also present important findings about Raman signatures of virus-related biomolecules that are utilized by the interpretable ML model for recognizing viruses. Testing the system using saliva and other clinical specimens will require an extensive study to determine how to control for background in various tissues. We will validate the method and the microfluidics device further in our future work.

Conclusions. In summary, we applied ML to identify viruses imaged by Raman spectroscopy. Our ML system, based on a CNN implementation, shows high accuracy in classifying different types of human and avian viruses. It can also differentiate subtypes of FLUA viruses. The interpretation of the NN responses also provides valuable information about Raman wavenumber ranges that correlate well with the signature ranges of known biomolecules and chemical functional groups present in viruses. The major contributions of our work are as follows:

(1) We developed a 1D-CNN classifier that achieved high accuracy for multiple virus identification and classification tasks, including differentiating enveloped from nonenveloped viruses, identifying types of human respiratory viruses, differentiating human FLUA from human FLUB viruses,

classifying subtypes of FLUA viruses, and differentiating among types of avian viruses.

(2) We further investigated the association between classifier-selected important Raman ranges and peak ranges of lipids, proteins, and relevant chemical functional groups and observed correlations that are consistent with existing knowledge.

(3) We delivered promising virus classification results that indicate Raman spectra of different virus types and subtypes contain recognizable Raman signatures that can be identified by ML models, which unravels the potential of using interpretable ML in a real-time virus surveillance system.

In our future work, we will collect more Raman spectra of different virus samples (human and animal, including DNA viruses) to build a large virus spectra database for training robust and highly accurate ML models. We will study virus evolution using temporal ML models trained on Raman spectra of virus strains of different types from different years and locations. And we will further improve the Raman enhancement with better signal intensities and lower noise levels, considering the feedback from ML classification and feature importance identification.

Materials and Methods

Virus Samples Preparation. Avian influenza virus (AIV) was propagated in specific-pathogen-free embryonating chicken eggs (ECEs) via allantoic cavity route inoculation at 9 to 11 d of age. The inoculated ECEs were incubated in a 37 °C egg incubator for 3 d (or 72 h) and then were removed/chilled at 4 °C for a minimum of 4 h or overnight. Allantoic fluid (AF) containing the virus was harvested from each egg using a sterile technique (a 3-mL sterile syringe with a 25G × 5/8″ needle). The harvested AF was clarified by centrifugation at 8,000 to 1,000 rpm for 10 min. Virus titer was determined in embryo infectious doses 50% (EID_{50}) titers by the Reed-Muench method (37). Briefly, the EID_{50} test was conducted in ECEs. The propagated fresh stock H5N2 AIV was prepared in 10-fold serial dilutions from 10^{-1} through 10^{-9}. Each dilution was inoculated into five eggs, 0.1 mL per egg. The inoculated eggs were incubated at 37 °C for 72 h. The eggs were candled daily to remove dead eggs to chill them at 4 °C refrigerator. After 72 h of incubation, AF was harvested from each egg (38).

H1N1, H3N2, FLUB, rhinovirus, and RSV were prepared in Madin-Darby canine kidney-London (MDCK-London) cell culture. MDCK-London cells were cultured in Dulbecco's modified Eagle's medium (Invitrogen, Carlsbad, CA), containing 10% fetal bovine serum and 1% penicillin-streptomycin, and incubated at 37 °C in a humidified CO_2 incubator.

Enteroviruses (CVB1, CVB3, EV70, EV71, or PV2) were propagated using HEK 293 cell lines. Infection of cells with enterovirus inoculum, harvesting of cells and media, and additional virus sample preparation steps are documented in the *Virus Propagation and Purification* subsection in Shingler et al. (39).

Virus Raman Spectra Data Acquisition. The VIRRION platform (4), constructed with nitrogen-doped CNT arrays and gold (Au) nanoparticles, was used as Surface enhanced Raman spectroscopy (SERS) substrate for collecting Raman spectra from virus samples. A 100 μL sample of each virus was directly dropped (drop-cast) onto the VIRRION Au-CNT substrate and air-dried at room temperature for 10 h prior to Raman measurements. Raman data acquisition was recorded using a Horiba-LabRAM HR Evolution system with a 785-nm diode laser line. The laser power on the sample was approximatley 3.6 mW, focused through a 100× objective. The 600 gr/mm grating was used with a spectral range from 500 to 2000 cm^{-1}. The typical acquisition time was 30 s.

Virus Raman Spectra Preprocessing Algorithm Details. First, we apply baseline correction with asymmetric least squares smoothing (15) to reduce background noise in spectra. This method estimates a polynomial baseline to correct baseline shift in Raman measurements. Then, we adjust the intensities that vary across the spectra of different virus types to a universal scale by normalization. In this step, we apply L_2 normalization that converts the input vectors to

unit vectors. The normalization makes intensities comparable across spectra and facilitates convergence during ML model training.

For generating the t-SNE plots of spectra data (Fig. 2 and *SI Appendix,* Fig. S1), we use the scikit-learn (40) ML package to perform the t-SNE dimensionality reduction and map high-dimensional data points to a 2D space. We use the default parameters of the package except for the perplexity value, which we set to 50, and we set the learning rate to 200. Under this setting of parameters, the data points in the 2D map for FLUA and FLUB spectra fall into clearly distinct clusters, which indicates that a deep learning network capable of nonlinear functional mapping should be able to achieve highly accurate classification on the dataset.

CNN Architecture and Training Details. As shown in Fig. 1B, the CNN for our task is built with four convolutional blocks. Considering the dimension of our training set is $N \times 1 \times D_w$, where N refers to the number of Raman spectra samples in the training set, and D_w is the dimension of Raman wavenumber range, a reasonable option for the convolutional blocks is to adopt 1D-CNN layer. Followed by the convolutional layer is a 1D batch normalization layer and an activation layer; in this case, we choose Rectified Linear Unit (ReLU). The kernel size and stride of the 1D-CNN layer of the first convolutional block are both set as 1, with the width fixed while increasing the depth from the input dimension 1 to the dimension of the hidden state, which will be specified later along with other hyperparameters. Next, for the other three convolutional blocks, kernel size is increased to 3, and stride is set as 2 for reducing the dimension of feature maps by half each time. Followed by the activation layer of the second and the third convolutional blocks, two dropout layers with rates 0.5 and 0.25 are applied, respectively, for alleviating overfitting to the training set. After all convolutional blocks, the last layer for obtaining the final classification results is a fully connected layer with output dimension as $N \times 1 \times D_c$, where D_c is denoted as the number of virus types or subtypes, depending on the classification task and specific dataset used for that task.

During training, we apply a 5-fold cross-validation and stratified sampling for each fold based on the virus types (or subtypes) to ensure that after splitting the dataset into training and testing sets, every type (or subtype) gets equal representation in both sets, regardless of how unbalanced the data distribution is. For fair comparison, we run the cross-validation five times and obtain the average score for all metrics across the five test runs. The corresponding performances reported in Fig. 4 are averaged results among the five hold-out test sets from cross-validation with error bars. Learning curves of the 5-fold cross-validation for the classification task on FLUA subtypes (H1N1/H3N2/H5N2/H7N2) are shown in *SI Appendix,* Fig. S10. The process of setting the hyperparameters was performed by manually fine-tuning and choosing the hyperparameters that gave good results for our 1D-CNN model. All hyperparameters are fixed for each run, and the learning rate is set as 0.001 and trained for 1,000 epochs with hidden dimension set to 128 for the first convolution block and then decreases by half for every subsequent convolution block. The Adam optimizer is used, and dropout rate is set as 0.2. Although systematic grid search for optimal hyperparameters was not needed in this work because the accuracy levels are relatively high already with the manually set hyperparameters, we expect that grid search optimization may be needed when we extend our dataset to include more viruses and larger sets of Raman spectra.

Calculation of Raman Feature Importance Map Using CNN Responses. While the CNN classifiers trained for virus identification tasks achieve high performance, we are interested in learning what Raman features are utilized by these classifiers to differentiate among viruses. To this end, we propose an algorithm for the CNN to infer the feature importance value for each specific wavenumber for further investigation of interpretability. With regard to the interpretation of feature extraction and selection by NNs, a saliency map has been widely considered as an intuitive and well-established method to visualize the importance value for each unit within the input data (22–27). However, in our case, the contributions each wavenumber have to the final virus type (or subtype) classification are highly unlikely to be independent from each other. A more reasonable assumption is that the distinguishable features from Raman spectra of a specific virus type (or subtype) are composed of a set of Raman signature ranges, besides individual wavenumbers of Raman spectra. Hence, a desirable design of saliency map representation for interpretation is expected to

include both attributions to ensure the completeness of the feature map. By leveraging features from input vector and neurons from intermediate layers simultaneously, the full-gradient algorithm (28) is proven to be a sensible representation of CNN interpretability in terms of the capability to capture both local and global attributions from each Raman spectra wavenumber and signature ranges. As the full-gradient representation for NN visualization (28) was originally designed and applied on natural images, we adapt and modify the full-gradient algorithm to accommodate the 1D vector inputs, as the format of Raman spectra is in our case. As shown in Fig. 1B, the process for extracting feature importance for each virus type or subtype is demonstrated below the architecture of CNN. The full-gradient feature importance map extracted is defined as

$$S_f(x) = \psi(\nabla_x f(x) \odot x) + \sum_{l \in L} \sum_{c \in c_l} \psi(\nabla_b f(x,b)_c \odot b).$$

Here, the saliency map of the full-gradient representation consists of two parts: input gradient that is specific to each wavenumber of Raman spectra in the training set and bias-gradient from each convolutional block. The components of each convolutional block are illustrated in Fig. 1B. The approximate networkwide representation of the feature map is considered comprehensive for capturing what the model learned throughout the process of the classification task from both lower and higher levels of abstraction. c refers to the virus type or subtype, depending on the target for a particular classification task. Gradients specific for each c are extracted separately in order to get insights of Raman frequency significance for different types or subtypes of viruses. This process is implemented by activating the virus type (or subtype) of interest during backpropagation through the entire set of convolutional blocks while obtaining the cross-entropy loss for each c. $\psi(\cdot)$ refers to the postprocessing steps that can be denoted as $\psi(\cdot) = \text{bilinearUpsample}(\text{normalize}(\text{abs}(\cdot)))$. First, the operation that is applicable for both input and bias gradients is the step of obtaining the absolute value of either positive or negative importance to visualize the significance while neglecting the sign. Next, the absolute values of gradients are normalized to the range of $[0, 1]$ to optimize the visualization by creating proper viewing contrast. Then, for the gradients extracted from convolutional blocks with dimension downsized to different scales of hidden states, we facilitate the aggregation of the blockwise feature maps by upsampling each to the same dimension as the input vector with bilinear interpolation. The feature map extracted for each virus type or subtype is shown in the format of the area chart in Fig. 1B.

Interpretable Raman Signatures. Considering that one of our goals is to make an educated guess as to which biomolecules are more likely to have a significant contribution in differentiating virus types or subtypes, we analyze the correlation between the important Raman ranges from CNN feature importance map and the Raman peak ranges of biomolecules existing in viruses. First, the Raman peaks of biomolecules including lipids, proteins, nucleic acids, and protein-related chemical functional groups are gathered from the literature (7, 8, 14) (SI Appendix, Fig. S9 for detailed peak ranges). We note that for a specific functional group, the specific Raman range can vary when measured in different environments. Here, we included all the possible Raman ranges for the generality of our analysis. For receptor-binding domain (RBD) proteins and amino acids (tyrosine, phenylalanine), we measured their Raman spectra in our own experiments and then located the peaks of the Raman spectra by adopting the python package (41). A shift of five wavenumbers is granted to each peak to

construct the peak ranges for each biomolecule (i.e., as a range for each peak). Second, given a Raman feature (i.e., wavenumber) importance map calculated using the full-gradient algorithm for CNN, we extract important Raman ranges by applying a threshold on the calculated feature importance values. We apply a Savitzky-Golay filter (42) on the relatively noisy importance values, with the length of the filter window set as 17. Then, a 40-percentile threshold is applied to extract ranges in the feature map that consist of wavenumbers with corresponding importance values above the threshold. Finally, the quantifiable metric–the matching score as demonstrated in Fig. 5–is used to measure the level of correlation between Raman peak ranges of biomolecules and important Raman ranges identified by ML. The matching score metric is developed in the format of a ratio, where the numerator of the ratio is the amount of overlap (i.e., number of overlapped wavenumbers) between the ML-calculated important Raman ranges for identifying a particular virus type and the Raman peak ranges of a certain biomolecule, and the denominator is the total number of wavenumbers in the biomolecule's peak ranges. Thus, the matching scores are in the range of [0,1]: a matching score of 1.0 means that the biomolecule's entire peak ranges are considered important by the CNN classifier for identifying the virus; a matching score of 0 indicates no wavenumber within the biomolecule's peak ranges is considered important by the classifier; and when the matching score value is between 0 and 1, the higher the score, the more likely that the biomolecule is important for identifying that particular type of virus. We report the matching scores for all our ML classification tasks in SI Appendix, Figs. S2–S7 and show the Raman peak ranges for biomolecules in SI Appendix, Fig. S9.

Author affiliations: aCollege of Information Sciences and Technology, The Pennsylvania State University, University Park, PA 16802; bDepartment of Physics, The Pennsylvania State University, University Park, PA 16802; cDepartment of Electrical and Computer Engineering, Johns Hopkins University, Baltimore, MD 21218; dDepartment of Electrical Engineering, The Pennsylvania State University, University Park, PA 16802; eDepartment of Biomedical Engineering, George Washington University, Washington, DC 20052; fSystems Genomics Section, Laboratory of Parasitic Diseases, National Institute of Allergy and Infectious Diseases, National Institutes of Health, Bethesda, MD 20894; gDepartment of Biochemistry and Molecular Biology, The Pennsylvania State University, University Park, PA 16802; hDepartment of Pathology and Laboratory Medicine, Division of Clinical Pathology, The Pennsylvania State University College of Medicine, Hershey, PA 17033; and iDepartment of Veterinary and Biomedical Sciences, The Pennsylvania State University, University Park, PA 16802

1. J. Paget et al.; Global Seasonal Influenza-associated Mortality Collaborator Network and GLaMOR Collaborating Teams*, Global mortality associated with seasonal influenza epidemics: New burden estimates and predictors from the GLaMOR Project. J. Glob. Health 9, 020421 (2019).
2. World Health Organization, Coronavirus disease 2019 (COVID-19): Situation report, 82 (2020). https://apps.who.int/iris/handle/10665/331780. Accessed 10 January 2021.
3. F. Keesing et al., Impacts of biodiversity on the emergence and transmission of infectious diseases. Nature 468, 647–652 (2010).
4. Y.-T. Yeh et al., A rapid and label-free platform for virus capture and identification from clinical samples. Proc. Natl. Acad. Sci. U.S.A. 117, 895–901 (2020).
5. S. Li et al., Noninvasive prostate cancer screening based on serum surface-enhanced Raman spectroscopy and support vector machine. Appl. Phys. Lett. 105, 091104 (2014).
6. A. Walter et al., From bulk to single-cell classification of the filamentous growing Streptomyces bacteria by means of Raman spectroscopy. Appl. Spectrosc. 65, 1116–1125 (2011).
7. K. Czamara et al., Raman spectroscopy of lipids: A review. J. Raman Spectrosc. 46, 4–20 (2015).
8. D. Němeček, G. J. Thomas Jr., "Raman spectroscopy of viruses and viral proteins" in Frontiers of Molecular Spectroscopy, J. Laane, Ed. (Elsevier, 2009), pp. 553–595.
9. J.-Y. Lim et al., Identification of newly emerging influenza viruses by detecting the virally infected cells based on surface enhanced Raman spectroscopy and principal component analysis. Anal. Chem. 91, 5677–5684 (2019).

10. D. Zhang et al., Ultra-fast and onsite interrogation of Severe Acute Respiratory Syndrome Coronavirus 2 (SARS-CoV-2) in environmental specimens via surface enhanced Raman scattering (SERS). bioRxiv [Preprint] (2020). https://doi.org/10.1101/2020.05.02.20086876. Accessed 20 January 2021.
11. Y. Liu et al., Label and label-free based surface-enhanced Raman scattering for pathogen bacteria detection: A review. Biosens. Bioelectron. 94, 131–140 (2017).
12. M. Reyes et al., Exploiting the anti-aggregation of gold nanostars for rapid detection of hand, foot, and mouth disease causing Enterovirus 71 using surface-enhanced Raman spectroscopy. Anal. Chem. 89, 5373–5381 (2017).
13. K. Moor et al., Noninvasive and label-free determination of virus infected cells by Raman spectroscopy. J. Biomed. Opt. 19, 067003 (2014).
14. Y. H. Ong, M. Lim, Q. Liu, Comparison of principal component analysis and biochemical component analysis in Raman spectroscopy for the discrimination of apoptosis and necrosis in K562 leukemia cells. Opt. Express 20, 22158–22171 (2012).
15. S.-J. Baek, A. Park, Y.-J. Ahn, J. Choo, Baseline correction using asymmetrically reweighted penalized least squares smoothing. Analyst (Lond.) 140, 250–257 (2015).
16. L. van der Maaten, G. Hinton, Visualizing data using t-SNE. J. Mach. Learn. Res. 9, 2579–2605 (2008).
17. C. Shorten, T. M. Khoshgoftaar, A survey on image data augmentation for deep learning. J. Big Data 6, 60 (2019).

18. G. James, D. Witten, T. Hastie, R. Tibshirani, *An Introduction to Statistical Learning: with Applications in R* (Springer, New York, NY, 2013).

19. T. Chen, C. Guestrin, "XGBoost" in *Proceedings of the 22nd ACM SIGKDD International Conference on Knowledge Discovery and Data Mining - KDD '16* (ACM Press, 2016). 10.1145/2939672.2939785.

20. L. Breiman, Random forests. *Mach. Learn.* **45**, 5–32 (2001).

21. J. M. Benitez, J. L. Castro, I. Requena, Are artificial neural networks black boxes? *IEEE Trans. Neural Netw.* **8**, 1156–1164 (1997).

22. M. D. Zeiler, R. Fergus, "Visualizing and understanding convolutional networks" in *Computer Vision – ECCV 2014*, Lecture notes in computer science, D. Fleet, T. Pajdla, B. Schiele, T. Tuytelaars, Eds. (Springer International Publishing, 2014), pp. 818–833.

23. K. Simonyan, A. Vedaldi, A. Zisserman, Deep inside convolutional networks: Visualising image classification models and saliency maps. arXiv [Preprint] (2013). https://doi.org/10.48550/arXiv.1312.6034. Accessed 1 May 2020.

24. J. Yosinski, J. Clune, A. Nguyen, T. Fuchs, H. Lipson, Understanding neural networks through deep visualization. arXiv [Preprint] (2015). https://doi.org/10.48550/arXiv.1506.06579. Accessed 20 May 2020.

25. R. R. Selvaraju et al., "Grad-CAM: Visual explanations from deep networks via gradient-based localization" in *2017 IEEE International Conference on Computer Vision (ICCV)*, (IEEE, 2017). 10.1109/iccv.2017.74.

26. P.-J. Kindermans et al., "The (Un)reliability of saliency methods" in *Interpreting, Explaining and Visualizing Deep Learning*, Lecture notes in computer science, D. Fleet, T. Pajdla, B. Schiele, T. Tuytelaars, Eds. (Springer International Publishing, 2019), pp. 267–280.

27. K. Zolna, K. J. Geras, K. Cho, Classifier-agnostic saliency map extraction. *Comput. Vis. Image Underst.* **196**, 102969 (2020).

28. S. Srinivas, F. Fleuret, "Full-gradient representation for neural network visualization" in *Proceedings of the 33rd Conference on Neural Information Processing Systems*, H. Wallach, H. Larochelle, A. Beygelzimer, F. d'Alché-Buc, E. Fox, R. Garnett, Eds. (NeurIPS 2019), Vol. 32.

29. C. E. McBride, C. E. Machamer, A single tyrosine in the severe acute respiratory syndrome coronavirus membrane protein cytoplasmic tail is important for efficient interaction with spike protein. *J. Virol.* **84**, 1891–1901 (2010).

30. S. Wang et al., AXL is a candidate receptor for SARS-CoV-2 that promotes infection of pulmonary and bronchial epithelial cells. *Cell Res.* **31**, 126–140 (2021).

31. F. Y. Shaikh et al., A critical phenylalanine residue in the respiratory syncytial virus fusion protein cytoplasmic tail mediates assembly of internal viral proteins into viral filaments and particles. *MBio* **3**, e00270-11 (2012).

32. C. J. Stewart et al., Respiratory syncytial virus and Rhinovirus bronchiolitis are associated with distinct metabolic pathways. *J. Infect. Dis.* **217**, 1160–1169 (2018).

33. J. Xu et al., Increased mortality of acute respiratory distress syndrome was associated with high levels of plasma phenylalanine. *Respir. Res.* **21**, 99 (2020).

34. R. W. Williams, Protein secondary structure analysis using Raman amide I and amide III spectra. *Methods Enzymol.* **130**, 311–331 (1986).

35. A. Rygula et al., Raman spectroscopy of proteins: A review. *J. Raman Spectrosc.* **44**, 1061–1076 (2013).

36. K. K.-W. To et al., Temporal profiles of viral load in posterior oropharyngeal saliva samples and serum antibody responses during infection by SARS-CoV-2: An observational cohort study. *Lancet Infect. Dis.* **20**, 565–574 (2020).

37. G. J. Ebrahim, Virology: Principles and applications. *J. Trop. Pediatr.* **55**, 66 (2007).

38. S. Zheng et al., Sizable tunable enrichment platform for capturing nano particles in a fluid. US Patent (2020). https://patents.google.com/patent/US20170038285A1/en.

39. K. L. Shingler et al., The enterovirus 71 A-particle forms a gateway to allow genome release: a cryoEM study of picornavirus uncoating. *PLoS Pathog.* **9**, e1003240 (2013). https://soundcloud.com/bangtan/sothatiloveyou?in=jiarong-ye/sets/bts-english-songs/s-vQqKYnTwhfl&utm_source=clipboard&utm_medium=text&utm_campaign=social_sharing

40. F. Pedregosa et al., Scikit-learn: Machine learning in Python. *J. Mach. Learn. Res.* **12**, 2825–2830 (2011).

41. P. Virtanen et al.; SciPy 1.0 Contributors, SciPy 1.0: Fundamental algorithms for scientific computing in Python. *Nat. Methods* **17**, 261–272 (2020).

42. W. H. Press, S. A. Teukolsky, Savitzky-Golay smoothing filters. *Comput. Phys.* **4**, 669 (1990).

43. J. Ye, Y.-T. Yeh, Dataset for "Accurate Virus Identification with Interpretable Raman Signatures by Machine Learning." Figshare. https://figshare.com/articles/dataset/pnas_dataset_csv/19426739. Deposited 15 April 2022.

44. J. Ye, Accurate Virus Identification with Interpretable Raman Signatures by Machine Learning. GitHub. https://github.com/karenyyy/Accurate-Virus-Identification-with-Interpretable-Raman-Signatures-by-Machine-Learning-. Deposited 15 April 2022.